

Global Precipitation Nowcasting of Integrated Multi-satellitE Retrievals for GPM: A U-Net Convolutional LSTM Architecture

Reyhaneh Rahimi^a, Ardeshtir Ebtehaj^{a,*}, Ali Behrangi^b, Jackson Tan^c

^a*Saint Anthony Falls Laboratory and Department of Civil Environmental and Geo-Engineering, University of Minnesota*

^b*Department of Hydrology and Atmospheric Sciences, The University of Arizona*

^c*Earth Sciences Division, NASA's Goddard Space Flight*

Abstract

This paper presents a deep learning architecture for nowcasting of precipitation almost globally every 30 min with a 4-hour lead time. The architecture fuses a U-Net and a convolutional long short-term memory (LSTM) neural network and is trained using data from the Integrated MultisatellitE Retrievals for GPM (IMERG) and a few key precipitation drivers from the Global Forecast System (GFS). The impacts of different training loss functions, including the mean-squared error (regression) and the focal-loss (classification), on the quality of precipitation nowcasts are studied. The results indicate that the regression network performs well in capturing light precipitation (below 1.6 mm hr^{-1}), but the classification network can outperform the regression network for nowcasting of precipitation extremes ($>8 \text{ mm hr}^{-1}$), in terms of the critical success index (CSI).. Using the Wasserstein distance, it is shown that the predicted precipitation by the classification network has a closer class probability distribution to the IMERG than the regression network. It is uncovered that the inclusion of the physical variables can improve precipitation nowcasting, especially at longer lead times in both networks. Taking IMERG as a relative reference, a multi-scale analysis in terms of fractions skill score (FSS), shows that the nowcasting machine remains skillful ($\text{FSS} > 0.5$) at the resolution of 10 km compared to 50 km for GFS. For precipitation rates greater than 4 mm hr^{-1} , only the classification network remains FSS-skillful on scales greater than 50 km within a 2-hour lead time.

Keywords: Remote Sensing, Precipitation, Passive Microwave, Global Precipitation

*Corresponding Author

Email address: ebtehaj@umn.edu (Ardeshtir Ebtehaj)

1. Introduction

Precipitation nowcasts, short-term forecasts with a lead time of fewer than 6 hours, are important for weather-dependent decision-making (Sun et al., 2014a; Ravuri et al., 2021; Shi et al., 2015; Otsuka et al., 2016, 2019) and early flood warning systems. Modern Numerical Weather Prediction (NWP) models, such as the NOAA’s Global Forecast System (GFS, Han and Pan (2011)) provide short-term predictions of near-surface global precipitation every one hour at resolution 0.25° (Toth and Kalnay, 1997; Sun et al., 2014a). However, operational applications of nowcasting by NWPs are often limited chiefly due to large uncertainties in initialization (Hwang et al., 2015), data assimilation techniques (Barker et al., 2004) as well sub-grid scale parameterization of convective processes (Zhang et al., 2021; Sun, 2005).

Initialization and data assimilation of NWPs often involve a spin-up period within which the forecast uncertainties are suboptimal (Buehner and Jacques, 2020; Lin and Pu, 2020; Lin et al., 2005). The typical spin-up period for a convection-permitting model is around 3–6 hours, making the forecast in this period highly uncertain (Kendon et al., 2021). Global forecast models are not often convective permitting (Prein et al., 2015) and rely on sub-grid scale parameterizations (Hohenegger et al., 2009; Kendon et al., 2012). These sources of uncertainty often lead to position errors in the prediction of the extent, intensity, and phase of precipitation events, especially when it comes to summertime mesoscale convective systems (Ban et al., 2014; Prein et al., 2015) and short-lived snowstorms (Liu et al., 2011).

Moreover, precipitation is not a basic state variable (e.g., velocity, temperature, and moisture distribution) in NWPs (Lin et al., 2015). Consequently, variational data assimilation frameworks rely on linear tangent models and their adjoint operators. Since precipitation processes have a flow-dependent non-linear relationship with the state variables, even with a carefully designed adjoint operator, the nowcast uncertainties can remain large (Errico et al., 2007; Zhang et al., 2013).

Experimental evidence has suggested that statistical post-processing and machine learning models can temporally extrapolate the observed precipitation fields by ground-based radars (Bowler et al., 2004; Ayzel et al., 2019) and spaceborne platforms (Otsuka et al.,

2016; Kumar et al., 2020) with a higher degree of accuracy than NWP, over a limited forecast lead time (Sønderby et al., 2020). The data-driven precipitation nowcasting models can be grouped into two classes. The first class often relies on classic regression (Germann and Zawadzki, 2002; Reyniers, 2008) or optimal estimation (Ayzel et al., 2019) while the second group often uses modern machine (ML) learning and artificial intelligence (AI) tools (Ravuri et al., 2021; Shi et al., 2015).

Among the first class of precipitation nowcasting models, the advective approaches (Bowler et al., 2004; Pulkkinen et al., 2019) attempt to track the near-surface wind velocity fields to predict the motion of the precipitating cells (Austin and Bellon, 1974) often using optical flow methods that infer motion patterns from previous consecutive frames of precipitation observations (Bowler et al., 2004, 2006). Utilizing this approach, different operational nowcasting models have been developed including the *Pysteps* (Pulkkinen et al., 2019) and the *rainymotion* (Ayzel et al., 2019).

The advective nowcast models can only represent a shifted version of previous observations, and the intensity of precipitation cannot be properly evolved (Agrawal et al., 2019). However, for example, the results in Lin et al. (2005) showed that the probability of precipitation detection is around 85 (50)% for an advection-based nowcasting model, compared with 50 (60)% for the Weather Research and Forecasting (WRF, Powers et al., 2017) model when the lead time is 1 (6) hour.

The second class of data-driven nowcasting models largely relies on deep learning neural networks (DNN, LeCun et al., 2015), primarily tailored for solving computer vision problems in image classification (Rawat and Wang, 2017), video frame prediction (Mnih et al., 2015; Yang et al., 2019), and semantic segmentation (McCormac et al., 2017). In summary, a sequence of observed precipitation fields serves as inputs/outputs of a DNN to train it as a nowcasting machine (Shi et al., 2015). Research suggests that nowcasting machines can provide more accurate predictions of convective heavy precipitation compared to the advective counterparts (Shi et al., 2015; Agrawal et al., 2019; Ravuri et al., 2021; Ehsani et al., 2021; Ma et al., 2022), largely due to their ability to learn complex nonlinear processes.

In one of the first attempts, a Convolutional LSTM (ConvLSTM) architecture was developed for precipitation nowcasting with a lead time of 90 minutes using radar-based images

over Hong Kong (Shi et al., 2015). Compared to the detective model by (Woo and Wong, 2014), this model has a higher correlation coefficient by 7% and a higher probability of detection by 5%. More recently, to extract spatial features of precipitation, a U-Net (Ronneberger et al., 2015) architecture is presented by Agrawal et al. (2019) for precipitation nowcasting at 1 km resolution and 1-hour lead time. The network was trained using a sequence of multi-radar multi-sensor (MRMS) precipitation over the United States without explicitly accounting for the temporal correlation of precipitation. This nowcasting model resulted in a precision of 80% in the detection of precipitation rates greater than 0.1 mm hr^{-1} and outperformed an advective-based optical flow model by Fleet and Weiss (2006) and NOAA’s numerical high-resolution rapid refresh predictions (HRRR) (Benjamin et al., 2016), which showed precision values of 50 and 70%, respectively. Furthermore, a deep generative neural network model for probabilistic nowcasting was developed by Ravuri et al. (2021), using radar data over the United Kingdom with a lead time of 30–90 minutes. The model showed improved performance than an advective nowcasting approach developed by Pulkkinen et al. (2019) for lead times longer than 30 minutes – especially in terms of capturing medium-to-heavy ($2\text{--}8 \text{ mm hr}^{-1}$) rainfall events.

Although most of the developed nowcasting models use ground-based regional precipitation radar observations (Han et al., 2021; Sun et al., 2014a; Pan et al., 2021), only recently a few studies have used satellite data to design nowcasting models based on advective techniques (Kotsuki et al., 2019; Otsuka et al., 2016) and ML methodologies (Kumar et al., 2020; Ehsani et al., 2022) for precipitation nowcasting. Based on a local ensemble transform Kalman filter, a prototype nowcasting system was implemented by Otsuka et al. (2016) and tested using the Japan Aerospace Exploration Agency’s Global Satellite Mapping of Precipitation (GSMaP) product (Kubota et al., 2007). More recently, Global Precipitation Measurement (GPM) Integrated Multi-satellitE Retrievals for GPM (IMERG, Huffman et al., 2020) satellite data were used over the eastern CONUS Ehsani et al. (2022) for training two types of neural networks, including a convolutional deep neural network and a recurrent neural network for precipitation nowcasting with 90 minutes lead time. The results showed that the DNN-based nowcasting outperforms an optical flow method (Fleet and Weiss, 2006) by improving the mean squared error.

In this paper, we present a Global prEciPitation Nowcasting using intEgrated multi-Satellite retrIevalS for GPM (GENESIS) by fusing a Convolutional LSTM (ConvLSTM, Shi et al., 2015) into a U-Net neural network (Ronneberger et al., 2015) and train it using IMERG observations (Huffman et al., 2020), as well as the GFS forecasts (GFS, Climate and Branch, 2003) of key drivers of precipitation in time and space. From a methodological point of view, the paper extends previous efforts through the following contributions. First, both temporal and spatial dependencies of global precipitation fields are accounted for through the LSTM and U-Net, respectively. Second, beyond the widely used mean-squared error loss function that can lead to an under-representation of precipitation extremes, we examine and document the functionality of focal loss function (Lin et al., 2017) that promises improved nowcasting of precipitation extremes.

It is important to emphasize that, the goal is to demonstrate the extent to which we can predict the sub-hourly evolution of the global precipitation field, considering IMERG as a relative and not an absolute reference observation. Therefore, we do not aim to quantify the intrinsic errors between GFS and IMERG data. However, the presented results are predicated on the presumption that the observational satellite data exhibit less uncertainty than the GFS predictions.

2. Inputs to the Nowcasting Machine

2.1. Data

As previously mentioned, the inputs to the nowcasting machine comprise a temporal sequence of IMERG product (Huffman et al., 2020), along with physically relevant variables from GFS by the National Centers for Environmental Prediction (NCEP, Climate and Branch, 2003). The half-hourly (hourly) IMERG (GFS) training data are collected from April 2020 to March 2023. The data over the first two years are used for training and the rest for testing of the nowcasting networks.

The IMERG optimally integrates estimates of passive microwave (Kummerow et al., 2015) and infrared (Hong et al., 2004) precipitation from the GPM constellation and geostationary satellites. The passive microwave precipitation is mostly processed by the Goddard PROFiling algorithm (GPROF, Kummerow et al., 2015) and propagated in time to be merged

with infrared precipitation (Hong et al., 2004), using a Kalman filtering approach (Joyce and Xie, 2011). The IMERG product provides gridded high-resolution estimates of precipitation rates globally with a spatial resolution of 0.1° every 30 minutes. However, some estimates at high latitudes may be missing due to the masking of passive microwave data over frozen surfaces. The product is available at three different time latencies: Early Run, Late Run, and Final Run. The first two sets of products are released with a time lag of 4 and 14 hours, respectively. The final run has a time latency of 3.5 months and its biases are adjusted using Global Precipitation Climatology Center (GPCC) monthly rain gauge analysis data (Schamm et al., 2014). For this study, sequences of half-hourly Early Run IMERG from V06 precipitation are used because of their minimum time latency. The networks can be updated after the release of V07, but the change in the results is expected to be insignificant.

The network is also fed with the NCEP’s GFS hourly (v16) forecasts (NCEP, 2021) with 0.25° resolution to further constrain the precipitation nowcasting. The forecast variables include near-surface horizontal wind velocity and total precipitable water content. The GFS includes an atmospheric model that is coupled with the Noah land surface model with multi-parameterization options (NoahMP, Niu et al., 2011), the Modular Ocean Model version 6 (MOM6, Adcroft et al., 2019), and the Los Alamos sea ice model (CICE6, Hunke et al., 2017).

The GFS atmospheric model uses the Finite Volume Cubed-Sphere Dynamical model (FV3) developed by the Geophysical Fluid Dynamics Laboratory (GFDL, Putman and Lin, 2007), which has replaced the Global Spectral Model (GSM) as the core model since June 2019. In the vertical dimension, there are 127 pressure levels with the top layer centered around 80 km height. The initial conditions for the global forecasts are obtained through the Global Data Assimilation System (GDAS, Abreu et al., 2012), which ingests various satellite and ground-based observations using a 4-Dimensional Incremental Analysis Update (Lorenc et al., 2015) data assimilation.

2.2. Preprocessing for Training

The question is how many sequences of IMERG are needed to be fed into the nowcasting machine. The answer to this question may be obtained through auto-correlation analysis.

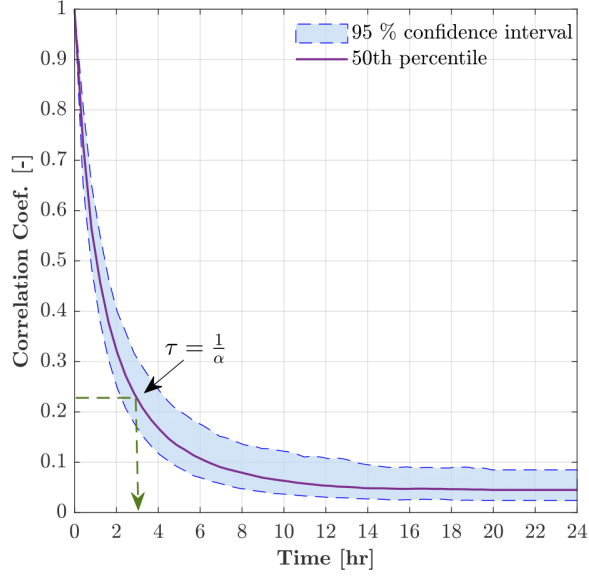


Fig. 1. Correlation coefficients between IMERG precipitation snapshots at different time lags with an exponential decay rate of $\alpha \approx 0.33 \text{ hr}^{-1}$.

Fig. 1 shows the median and 95% confidence bound of the temporal correlation at different time lags for 1,000 randomly selected 48 sequences of IMERG over a 24-hours time window.

The analysis shows that the correlation decays almost exponentially in time with a rate of $\alpha \approx 0.33 \text{ hr}^{-1}$, equivalent to a correlation length of $\tau = 1/\alpha \approx 3 \text{ hr}$. As is evident, after 6 hours the median of the coefficients is around 0.1 and reaches a plateau of 0.05 after approximately 12 hours. Therefore, it appears that after 6 to 8 hours, the global precipitation fields have minimal memory of the past, even though a negligible long-term dependency appears to persist. Given this information and the computational complexity of the problem, we confine our considerations to a time window of six hours for nowcasting the next four hours every 30 minutes.

As noted previously the network not only learns from the past IMERG data but also constrains its solutions to the available GFS forecasts of total precipitable water (TPW) [kg m^{-2}], as well as the horizontal U , and vertical V velocity fields 2-meter above the surface [m s^{-1}]. We used a nearest-neighbor interpolation to map the GFS data onto the IMERG grids to be able to organize the training data sets over the same domain.

Suppose a dynamical system is represented over an $M \times N$ grid. Inside each grid pixel at

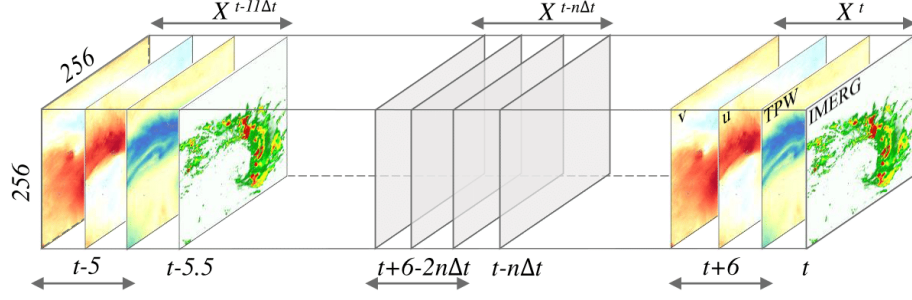


Fig. 2. A schematic of a block of twelve input tensors $X^{t-n\Delta t}$ over 6 hours with $n = 0, \dots, 11$ – organized for training the nowcasting machine with $\Delta t = 1/2$ hr. The tensors contain past IMERG precipitation as well as past and future GFS data of total precipitable water (TPW) and near-surface horizontal wind velocities U and V .

time t , there are C predictors stored among multiple channels including IMERG precipitation P , TPW , U , and V . Thus, the predictors at time t can be represented by a tensor $X^t \in \mathbb{R}^{M \times N \times C}$, where $C = 4$. Unlike IMERG precipitation, GFS forecasts are available on an hourly time scale. Therefore, for twelve past sequences of IMERG, we use six past and future sequences of GFS data and organize them for training as follows:

$$\begin{aligned}
 X^t &= [P^t | TPW^{(t+12\Delta t)} | U^{(t+12\Delta t)} | V^{(t+12\Delta t)}] \\
 X^{(t-\Delta t)} &= [P^{(t-\Delta t)} | TPW^{(t+10\Delta t)} | U^{(t+10\Delta t)} | V^{(t+10\Delta t)}] \\
 &\vdots \\
 X^{t-n\Delta t} &= [P^{(t-n\Delta t)} | TPW^{(t+6-2n\Delta t)} | U^{(t+6-2n\Delta t)} | V^{(t+6-2n\Delta t)}]
 \end{aligned} \tag{1}$$

where $n = 0, 1, \dots, 11$ with $\Delta t = \frac{1}{2}$ hr. By stacking the multiple tensors over 6 hours, we have the entire training block of input predictors as $\mathcal{X} = [X^t | X^{t-\Delta t} | \dots | X^{t-11\Delta t}] \in \mathbb{R}^{M \times N \times C \times T}$. This input block of data is fed into the network to predict the most likely output tensor $\mathcal{Y} = [P^{t+\Delta t} | P^{t+2\Delta t} | \dots | P^{t+8\Delta t}] \in \mathbb{R}^{M \times N \times T_f}$ that contains the next 4 hours of future IMERG precipitation such that $\mathcal{Y} = f(\theta, \mathcal{X}) : \mathbb{R}^{M \times N \times C \times T} \rightarrow \mathbb{R}^{M \times N \times T_f}$, where θ denotes all the unknown network parameters.

A tensor of the input data to the nowcasting machine is sketched in Fig. 2. Here, we choose $M = N = 256$ for computational amenability. The outputs are then tiled with 50% overlap and only 128×128 interior pixels are used to reconstruct the entire domain of IMERG. Overall, 100,000 patches of tensor blocks were randomly sampled over the spatial

domain of the problem from April 2020 to March 2022. This data set was split into 70 and 30% for training and validation. For testing 15,000 independent random samples were used from April 2022 to March 2023.

3. Methodology

3.1. Network Architecture

As previously noted, the used architecture fuses two U-Net (Ronneberger et al., 2015) and Convolutional LSTM (ConvLSTM, Shi et al., 2015) neural networks. The U-Net consists of a contracting path known as an encoder to capture fine-scale low-level spatial features of the inputs and a symmetric expanding path or a decoder that enables precise localization and construction of high-level output features. In order to propagate localized contextual information to high-resolution layers, skip connections are used that append the low-level features in the encoder blocks to the upsampled high-level features in the decoder blocks. Such connections help the model to learn more efficiently and to converge much faster in the training stage while alleviating the vanishing gradient problem (LeCun et al., 2015). Evidence suggests that the U-Net can converge fast even with a few numbers of training samples and without substantial loss of resolution due to the effects of the skip connections (Ronneberger et al., 2015). However, U-Net architecture is primarily designed to learn spatial features of static fields and has no specific mechanisms for capturing long-term dependencies in data sequences (Wang et al., 2022).

For time series modeling, LSTM networks are specifically designed to extend the predictive skills of classic Recurrent Neural Networks (RNN) for general sequenced data or time series with long-range dependencies (Hochreiter and Schmidhuber, 1997). The major innovation of LSTM stems from its memory cells. These cells enable the network to maintain a memory of important dependencies and propagate the error information over a sufficiently long window of time for updating its parameters without the vanishing and/or exploding gradients problems (Hochreiter and Schmidhuber, 1997; Graves, 2013). However, LSTMs need to cope with too many redundancies in their parameterization that render them ineffective in processing temporal dependencies of spatially high-dimensional data. To overcome this inefficacy, the Convolutional LSTM (ConLSTM) cell is introduced by Shi et al. (2015) in

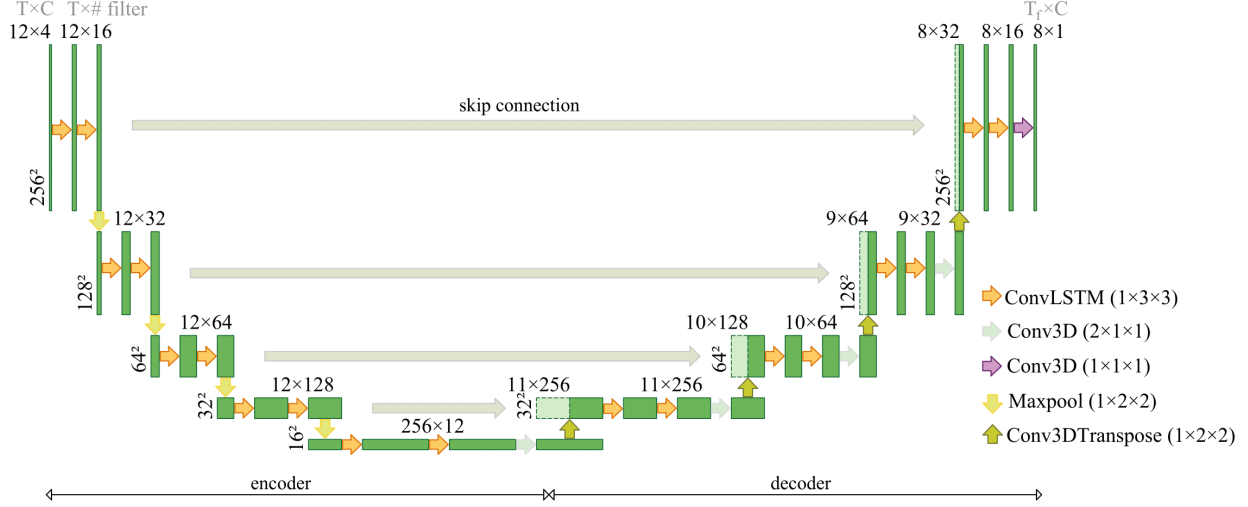


Fig. 3. Schematics of the nowcasting machine. An encoder operates on a sequence of input data, through a series of convolutional LSTM kernels to extract their low-dimensional spatiotemporal features and then a decoder upsamples the features through a series of deconvolution to reconstruct the evolution of precipitation fields. Note that the outcome of the contracting and expanding paths lead to learning from $T = 12$ sequences of input tensors to produce $T_f = 8$ sequences of output precipitation over a 4-hour lead time.

which large-scale matrix-vector multiplications are substituted by computationally efficient convolution operations.

The architecture of the IMERG nowcasting network is shown in Fig. 3, where the sizes of the kernels are reported as a legend. Each encoder block is composed of two ConvLSTM layers followed by a Rectified Linear Unit (ReLU) activation function, a max pooling down-sampling layer, a batch normalization, and a 15% dropout layer. Each decoder block consists of a 3D transposed convolution operator, a concatenation with the corresponding encoder block through the established skip connections, followed by two sets of ConvLSTM blocks, a 3D temporal convolution(Conv3D), a batch normalization, and a dropout layer.

3.2. Loss Functions

Due to the presence of convolution operators in the network architecture, it is expected that the output fields to be more blurred than the inputs, leading to an under-representation of precipitation extremes. The choice of the loss function can impact the significance of the blurring effects. There are multiple sets of loss functions that can be tested for this purpose including the mean squared or absolute error losses, Wasserstein distance (Villani et al.,

2009), and those loss functions that are often used for classification problems such as the cross entropy (MacKay and Mac Kay, 2003) and focal loss functions (Lin et al., 2017).

Commonly used loss functions such as the mean-squared error (MSE) are known to lead to blurred results and lack the ability to respect the non-Gaussian probability distribution of the precipitation (Guilloteau et al., 2023; Ehsani et al., 2021). Another approach is to discretize the input-output rates of precipitation into a finite number of intervals and recast the nowcasting into a multi-class classification problem. The main advantage of the latter approach is that by defining the nowcasting as a classification problem the network would attempt to implicitly reconstruct the precipitation histogram rather than minimize the second-order statistics of the nowcasting error.

As a commonly used loss function for classification tasks, cross-entropy measures the dissimilarity between two discrete probability distributions or more precisely the amount of information needed to encode the reference distribution, given the predicted distribution. However, cross-entropy loses its performance when there is a high imbalance between classes. In this scenario, the majority of class examples (easy to classify) will dominate the value of the loss function, causing the weights to be updated in a direction that the network becomes less and less skillful in predictions of less frequent classes (hard to classify). In the case of precipitation nowcasting, as a dynamic semantic segmentation problem, each patch of the precipitation field is dominated by non-precipitating areas which are easy to classify, and only limited areas are often covered by light-to-heavy precipitating. These precipitating areas become harder to classify for higher rates. The reason is that by discretizing precipitation, those classes, populated with heavier precipitation rates, become less and less frequent due to its positively skewed distribution.

The focal loss function extends the cross-entropy for imbalanced classification tasks. Conceptually, it shifts the focus from easy-to-classify pixels toward hard-to-classify ones. This is achieved first by scaling the cross-entropy function by a focusing parameter that prevents the loss from being overwhelmed by the easy-to-classify pixels. Second, it balances the contribution of each class to the total loss by a weighting factor. The categorical focal loss (FL) for a multi-class classification problem is defined as follows (Lin et al., 2017):

$$\text{FL}(y, p) = -\frac{1}{N} \sum_{i=1}^N \sum_{c=1}^C \alpha_c y_{i,c} (1 - p_{i,c})^\gamma \log p_{i,c} \quad (2)$$

where $y_{i,c}$ and $p_{i,c}$ are the reference and predicted probabilities of c^{th} class for i^{th} training data point with $i = 1, \dots, N$. The parameter α_c is a weight factor that balances the number of data points in different classes and γ is the focusing parameter. The values of α_c are often set proportional to the inverse of the frequency of occurrence in each class such that $\sum_c \alpha_c = 1$ and γ ranges from 2 to 5. The larger values of γ put more emphasis on the role of the less frequent or hard-to-classify data points in the total loss.

We use both mean-squared error and focal loss ($\gamma = 2$) functions for training the GENESIS, referred to as GENESIS_{MSE} and GENESIS_{FL} throughout the paper, respectively. To train the classification network, the output precipitation rate is discretized into 10 classes in a logarithmic scale ranging from 0.1 to 32 mm hr⁻¹. Rates below (above) 0.1 (32) mm hr⁻¹ are assigned to class 1 (10). To obtain the optimal weight of the network, the Adam optimizer (Kingma and Ba, 2014) is employed with an adaptive learning rate. To initialize the weights of the nowcasting networks, the *Xavier* method (Sun et al., 2014b) is used, which helps to alleviate the vanishing or exploding gradient problem during the training. The learning rate $\eta=1\text{E-}3$ and the mini-batch size 8 were found to provide reasonable results. A decay factor of 0.1 is set for the learning rate at every 10 epochs if there is no improvement in the validation loss. The network is trained using the TensorFlow-V2 library (Abadi et al., 2016) on an AMD EPYC 7542 32-Core central processing unit with 1008 GB of random access memory equipped with an NVIDIA A-100 40-GB graphical processing unit, provided by the Minnesota Super Computing Institute (MSI).

3.3. Nowcasting Quality Metrics

To assess the nowcasting performance, common categorical evaluation metrics were used including precision $TP/(TP+FP)$, recall $TP/(TP+FN)$, Heidke skill score (HSS, Jolliffe and Stephenson, 2012), and critical success index (CSI_r , $TP/(TP+FN+FP)$, (Schaefer, 1990)) – in which the true positive (TP), true negative (TN), false positive (FP), and false negative (FN) rates characterize the confusion matrix. Furthermore, to compare the performance of

the models at different spatial scales, fractions skill score $FSS = 1 - \frac{\sum_{i=1}^M (S_f^i - S_{obs}^i)^2}{\sum_{i=1}^M (S_f^i)^2 - \sum_{i=1}^M (S_{obs}^i)^2}$ is used in which S_f and S_{obs} are fractional coverage values of the forecasts and observations for M selected spatial windows with a spatial scale of interest (Ayzel et al., 2020).

To quantify the dissimilarity between the observed and predicted probability distribution of precipitation classes the Wasserstein distance (Villani et al., 2009) is used. This metric is derived from optimal transport theory, which considers the problem of quantifying the cost of morphing one distribution into another one non-parametrically. The cost defines a distance metric that not only penalizes the shifts between the mean of the distributions (bias) but also the misshape in terms of all higher-order moments. Clearly, smaller values of this metric denote that the two densities are closer in terms of their central locations and shapes. For further information, the readers are referred to (Ning et al., 2014; Tamang et al., 2020) in the context of geophysical data assimilation and climate model comparisons (Vissio et al., 2020; Robin et al., 2017).

The value of precision, recall, CSI_r , and FSS can vary from 0 to 1 with a perfect score of 1. The values of HSS vary from $-\infty$ to 1 indicating the worst and the best forecasts while positive values denote better than a random prediction. It should be recalled that in the CSI_r index, the elements of the confusion matrix are determined for a binary representation of the precipitation fields with the rates above a prespecified threshold r in mm hr^{-1} . To evaluate the performance of the regression network using categorical scores, the predicted rates are converted to the same classes defined for the classification network.

4. Results and Discussion

4.1. Storm-scale Nowcasting

Figure 4 shows the nowcasting results of Hurricane Ian initialized at 20:00 UTC on 27 September 2022. Visual inspection indicates that the presented nowcasting machine can predict the storm space-time dynamics. Overall, the GFS predictions are less coherent than IMERG and lack the prediction of some heavy precipitation cells. The extent of the storm in GFS is larger than the IMERG. There are high-intense cells in IMERG, organized in the storm band structures, that do not manifest themselves in GFS. This is partly expected as

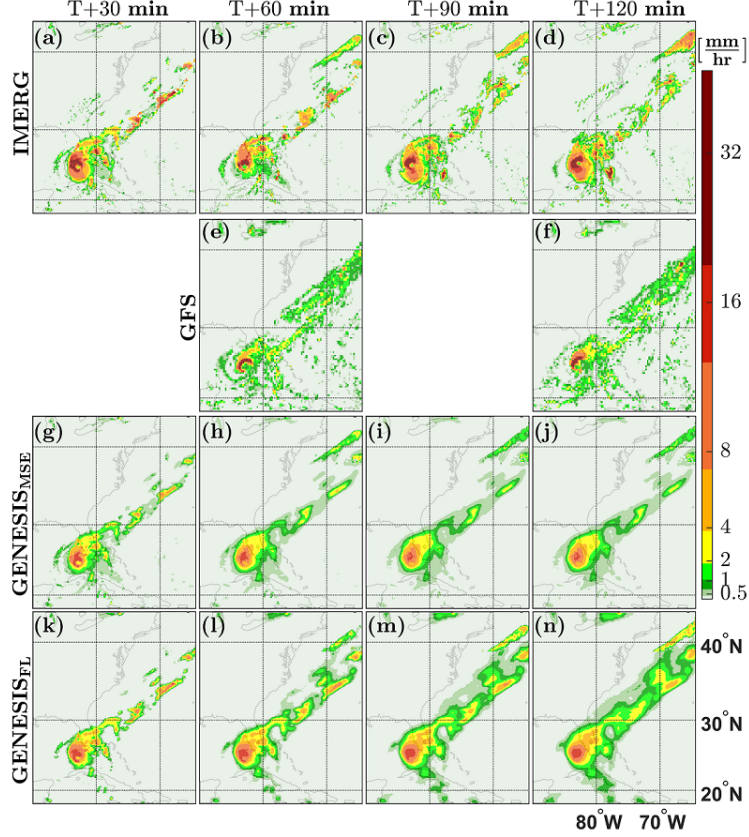


Fig. 4. Evolution of the Hurricane Ian over 2 hours, with a timestep of 30 min, beginning at 20:00 UTC on September 27, 2022, by IMERG (a–d), GFS (e–f), GENESIS_{MSE} (g–j), and GENESIS_{FL} (k–n).

the GFS spatial resolution is coarser than the IMERG. The difference in capturing high-intense cells is not only apparent over the rainbands around the eyewall but also over those extended outer bands, for example near the coasts of South Carolina at the 4th time-step. The nowcasting machine seems to produce precipitation fields that are expectedly consistent with the IMERG observations, even though some underestimations are apparent – especially over long lead times due to repeated applications of convolution and max-pooling operations.

Comparing the performance of the GENESIS_{MSE} and GENESIS_{FL} reveals that at time $T+30$ min both models capture some detailed structures of the observed storm, although the GENESIS_{MSE} underestimates the rates to a larger extent. By $T+60$ min, it becomes apparent that the use of the focal-loss function can lead to improved preservation of precipitation extremes when compared to its regression counterpart. It is worth noting that both nowcasts are perceptually closer to the IMERG observations than GFS forecasts. For example, an

outer rainband manifests itself near the coast of New York and intensifies over longer time steps. This rain band is missed in GFS forecasts; however, is detected and evolved in the nowcasting precipitation products. For longer lead times, the classification network shows a tendency to preserve the precipitation extremes at the expense of overestimating the extent of the storm.

		Lead Time							
Metric	Model	$T + 30$	+60	+90	+120	+150	+180	+210	+240
CSI_1	GFS		0.25		0.25		0.26		0.28
	MSE	0.71	0.63	0.59	0.52	0.40	0.36	0.34	0.33
	FL	0.69	0.61	0.57	0.53	0.43	0.40	0.37	0.37
CSI_8	GFS		0.14		0.24		0.18		0.12
	MSE	0.24	0.26	0.26	0.26	0.27	0.22	0.17	0.14
	FL	0.53	0.41	0.33	0.35	0.33	0.32	0.28	0.29

Table 1: Critical success index of regression ($\text{GENESIS}_{\text{MSE}}$), and classification ($\text{GENESIS}_{\text{FL}}$) networks as well as GFS against IMERG observations at threshold 1 and 8 mm hr⁻¹ for the storm shown in Fig. 4.

Table 1 presents the critical success index (CSI_r) with two different precipitation rates $r = 1$ and 8 mm hr⁻¹ over the entire 4-hour lead time. The results indicate the CSI values for GFS forecasts remain around 0.25 for $r = 1$ mm hr⁻¹ and vary between 0.14 to 0.24 for $r = 8$ mm hr⁻¹. For the nowcasting machines, the CSI_1 score decreases approximately from 0.7 to 0.3 when the lead time grows. The CSI_1 score is slightly higher for the $\text{GENESIS}_{\text{MSE}}$ than the $\text{GENESIS}_{\text{FL}}$ over lead times less than 90 minutes and then the $\text{GENESIS}_{\text{FL}}$ gradually overtakes the $\text{GENESIS}_{\text{MSE}}$ for longer lead times. For $r = 8$ mm hr⁻¹, $\text{GENESIS}_{\text{FL}}$ seems to provide a superior nowcast quality than $\text{GENESIS}_{\text{MSE}}$, even though, the difference tends to shrink from 0.27 at $T + 60$ min to 0.15 at $T + 240$ min.

4.2. Multi-storm Nowcasting

To provide a more comprehensive evaluation of the nowcasting machines, we randomly selected 15,000 independent samples of input-output tensor blocks, from April 2022 to March 2023 and use them for nowcasting and calculation of the forecast quality metrics. Four

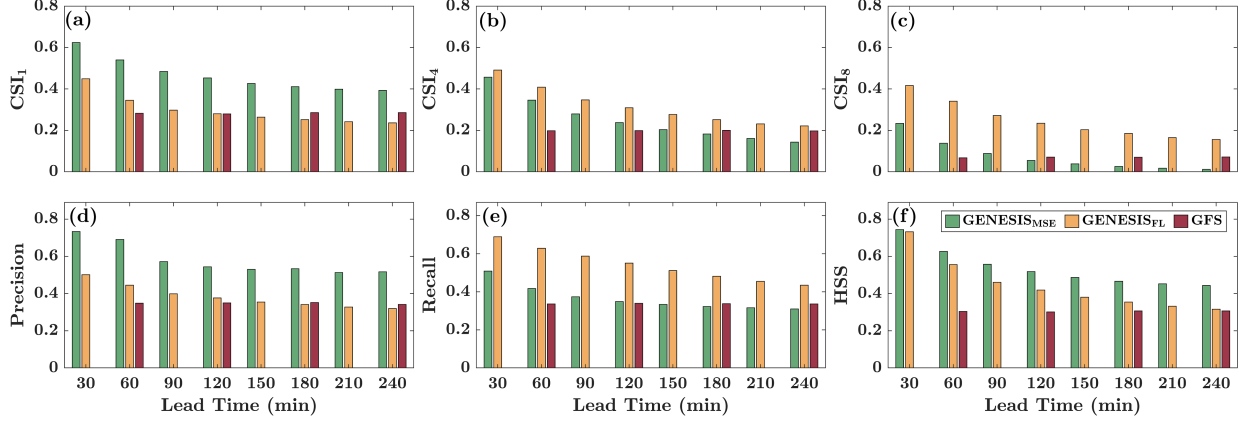


Fig. 5. Ensemble mean of (a) CSI_1 , (b) CSI_4 , (c) CSI_8 , (d) precision, (e) recall, and (f) HSS for regression ($GENESIS_{MSE}$), classification ($GENESIS_{FL}$), and GFS forecasts using 15,000 independent input samples from the test set.

different metrics including CSI_r at three threshold values, precision, recall, and HSS are calculated for each sample, and their ensemble mean is presented in Fig. 5 for different lead times.

Figure 5a shows the CSI_1 for all three nowcasts. The GFS performance is fairly stable over different lead times and remains around 0.3. However, CSI_1 for regression (classification) network reduces from 0.6 to 0.4 (0.45 to 0.2) when lead time increases from $T + 30$ min to $T + 240$ min. This difference can be attributed to the imbalanced nature of the data and improved skills of the regression network to represent the bulk of the precipitation distribution.

By increasing the CSI threshold to a precipitation rate of 4 mm hr^{-1} (Fig. 5b), the performance of GFS forecasts reduces by 30%, from 0.30 to 0.20, at $T + 60$ min but still remains fairly invariant with the lead time. However, the performance of the regression network decays by a factor of 3, from 0.45 to 0.15, when lead time increases from $T + 30$ min to $T + 240$ min. Meanwhile, the CSI_4 in the classification network decays from 0.49 at $T + 30$ min to 0.22 at $T + 240$ min, showing that this network begins to outperform the regression network by capturing higher intensity precipitation rates at longer lead times.

For more intense precipitation (Fig. 5c), the results indicate that the value of CSI_8 for GFS, $GENESIS_{MSE}$, and $GENESIS_{FL}$ models decay by 70, 60, and 15 % at $T + 60$ min

compare to CSI_4 , respectively. This metric, for the regression network, has its highest value of 0.23 at $T+30$ min and vanishes to almost zero after $T+150$ min. Meanwhile, the classification network still shows some skills and a potential to accurately capture precipitation rates above 8 mm hr^{-1} as CSI_8 is around 0.4 (0.15) at $T+30$ ($T+240$) min. It should be noted that the CSI_8 is low for all predictions and never exceeds 40%, for the regression network. This lack of skill may be attributed to a significant level of spatial smoothing due to the use of the mean-squared-error loss function, which becomes more pronounced as the lead time grows.

Figure 5d shows the precision metric for different lead times. Precision is a categorical metric that explains the number of truly detected precipitating events divided by all detected precipitating events. Clearly, this metric can be defined for different ranges of precipitation rates as defined in Sec. 3. The precision value for GFS remains constant in time around 0.35. For the regression (classification) network, it is around 0.75 (0.5) at the first lead time and decays by 20% (30%) to 0.5 (0.35) at the fourth time step and then remains relatively constant for longer times. The reason for the regression network having higher mean precision than the classification one is that this network better captures the body of precipitation distribution and low-intensity events with a rate less than 1 to 1.5 mm hr^{-1} . Although the difference between the precision of the two nowcasting models for classes with higher intensity values is not significant (not shown here).

The recall metric (Fig. 5e) shows the ratio of the number of correctly classified sample points to the total observations, which can be defined for each class. The recall value of GFS forecasts remains invariant with time and has a constant value of around 0.35. The regression network has a value equal to 0.5 at the first time step which reduces by a factor of 1.5 at the sixth lead time and remains relatively constant around 0.3. Meanwhile, the metric for the classification network is around 0.7 (0.50) at $T+30$ ($T+180$) min. The reason can be attributed to the higher skills of this network in detecting precipitation rates greater than 4 mm hr^{-1} with a lower value of false negative. In terms of HSS (Fig. 5f), it can be stated that all three schemes are performing better than a random chance by having the HSS value above zero. Particularly, the GFS forecasts show a time-invariant HSS of around 0.30. While both regression and classification networks have high HSS values of 0.75 at $T+30$ min, which are reduced to 0.45 and 0.31 at $T+240$ min, respectively.

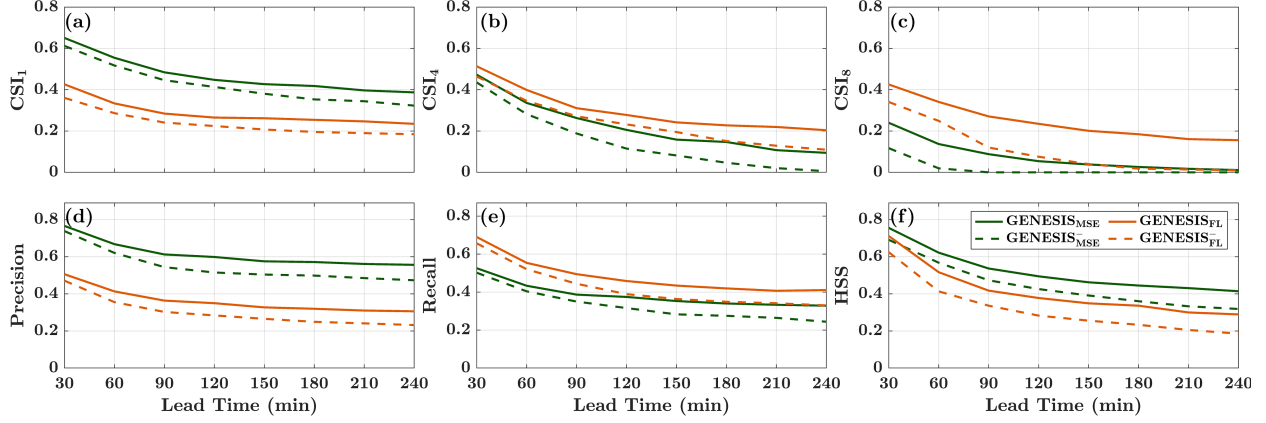


Fig. 6. Ensemble mean of (a) CSI_1 , (b) CSI_4 , (c) CSI_8 , (d) precision, (e) recall, and (f) HSS for 15,000 independent samples from the test set for nowcasting machines equipped with MSE $GENESIS_{MSE}$ and focal-loss function $GENESIS_{FL}$ with (solid lines) and without (dashed lines) inclusion of GFS physical variables in the training process.

4.3. Impacts of Physical Variables

To quantify the impacts of forecast variables on the performance of the nowcasting machines, we trained identical networks using only sequences of IMERG precipitation (denoted as $GENESIS^-$) and compared the outputs with those that are informed by the GFS forecasts as well, using both regression and classification loss functions. Overall, it can be stated that including past and future physical variables in the training can improve the nowcasting skill, especially at longer lead times.

Figure 6 a shows variation of CSI_1 over 4-hours lead time. It can be seen that adding the information content of the GFS physical variables improves the nowcasting skill of the regression (classification) models for precipitation rates greater than 1 mm hr^{-1} by 7 (16)% at $T + 30$ and by 18 (20)% at $T + 240$ min. However, at higher CSI thresholds of 4 and 8 mm hr^{-1} (Fig. 6 b–c), the gains become more significant.

Figure 6 b, shows that for both $GENESIS$ networks at $T + 30$ min, the CSI_4 value without and with GFS inputs are close to each other; however, the difference increases to almost 0.1 at $T + 240$ min. The effects of using physical variables become more pronounced in predicting more intense precipitation at longer lead times (Fig. 6 c) as in the classification (regression) network, the CSI_8 increases from 0.34 to 0.43 (0.12 to 0.23) at $T + 30$ min when physical variables are used in the training. Additionally, the figure shows that without the inclusion

of physical variables, the classification network does not have any skill in predicting high-intensity precipitation after $T + 180$ min while the physically informed network has CSI_8 value around 0.15 at that lead time. The skillful lead time for the regression network, with no physical variables, reduces to $T + 60$ min while the physically informed network has CSI_8 value of around 0.13.

The variation of precision (Figure 6 d) at different lead times shows that the inclusion of physical variables in the regression (classification) network causes precision to increase by 3% (6%) at the first time-step and by 17% (30%) at the last time-step. Additionally, the improvement in recall (Fig 6 e) grows with the lead time, from $T + 30$ min to $T + 240$ min, by 30 (18)%. In terms of the HSS metric (Fig. 6 f), the same pattern is observed showing that all models are performing better than random chance and utilizing physical variables can improve the nowcasting skill by at least 5%.

4.4. Multi-scale Analysis of the Nowcasting Performance

In this subsection, we aim to use FSS to provide further insights into the dependency of the nowcasting skills on both spatial scales and the precipitation exceedance thresholds. As previously explained, this score is obtained by comparing the predicted and reference fractional coverage of precipitation rates, above a certain threshold, within a spatial window defined by a particular scale. The FSS values of greater than $0.5 + f/2$ are commonly considered skillful where f is the fraction of the observed grid-box events in the full domain (Skok and Roberts, 2016). Thus if f tends to zero, a value of 0.5 can be considered as a lower limit (Mittermaier and Roberts, 2010). Figure 7 shows the mean values of FSS for GFS, GENESIS_{MSE}, and GENESIS_{FL} obtained over 15,000 independent randomly sampled test events, for spatial window sizes of $s = 10, 50, 100$, and 500 km, and intensity thresholds of 0.5, 1, 4, and 8 mm hr⁻¹.

As expected, the FSS skills decrease with decreasing spatial scales, increasing lead times, and increasing intensity thresholds. As shown in Fig. 7 a–c, once again, the GFS skill is not significantly a function of lead time and remains skillful only for intensity threshold of 0.5 and 1 mm hr⁻¹ at scales greater than 50 km. Note that at these intensity thresholds, the main body of the precipitation distribution is dominated by light values which are easier to

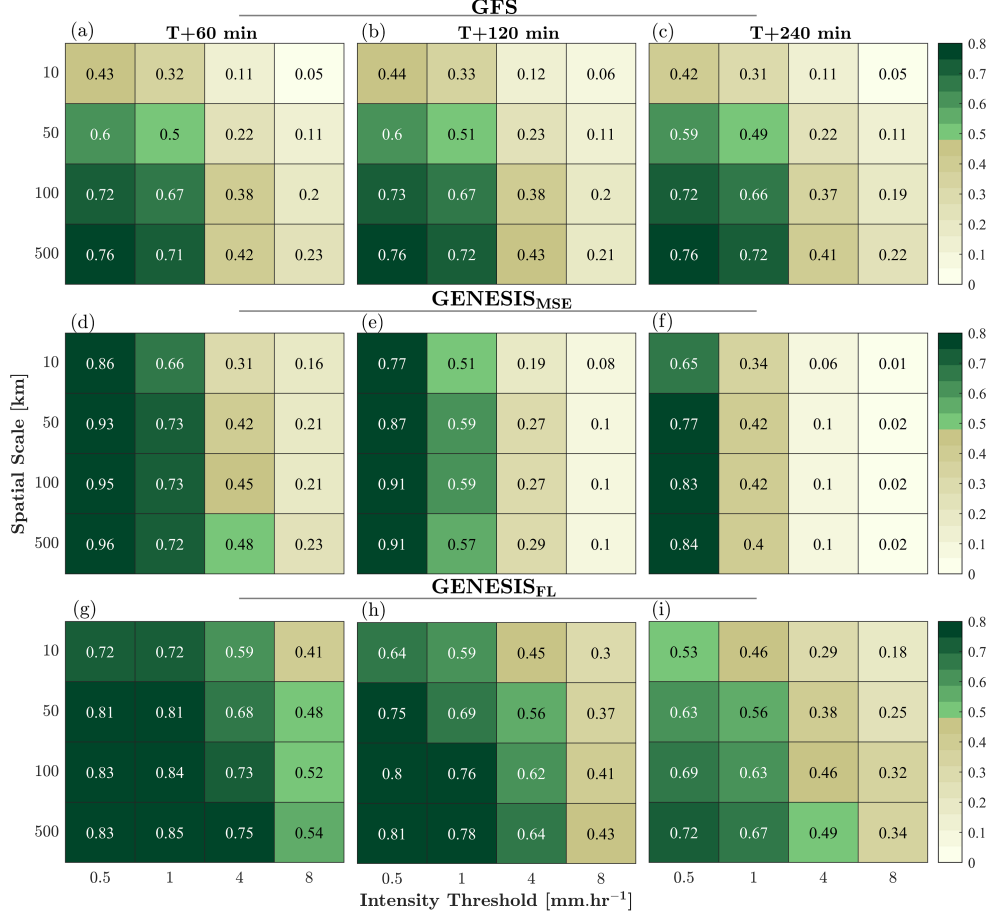


Fig. 7. Fractions skill scores (FSS) for GFS (a–c), GENESIS_{MSE} (d–f), and GENESIS_{FL} (g–i) at 60, 120, and 240 minutes lead times over spatial window sizes of 10, 50, 100, and 500 km for intensity thresholds of 0.5, 1, 4, and 8 mm hr⁻¹.

capture. By increasing the scale from 50 to 500 km the skillful FSS values increase roughly from 0.5 to 0.7 across the examined lead times. As expected, the GFS does not show any skill at the native IMERG resolution of 10 km.

Figures 7d–f indicate that the regression network remains spatially skillful at the native IMERG resolution 10 km when the intensity threshold is 1 (0.5) mm hr⁻¹ at the 2-hour (4-hour) lead time. However, its performance becomes gradually worse than GFS for heavier precipitation and longer lead times. For example, at a scale of 100 km and rates greater than 1 mm hr⁻¹, the GFS exhibits a skill of 0.66; however, the skill of the regression network is around 0.42. While the regression network remains skillful at $T + 120$ minute at rates greater than 1 mm hr⁻¹ at all spatial scales, unlike GFS, it loses its skills at a 4-hour lead

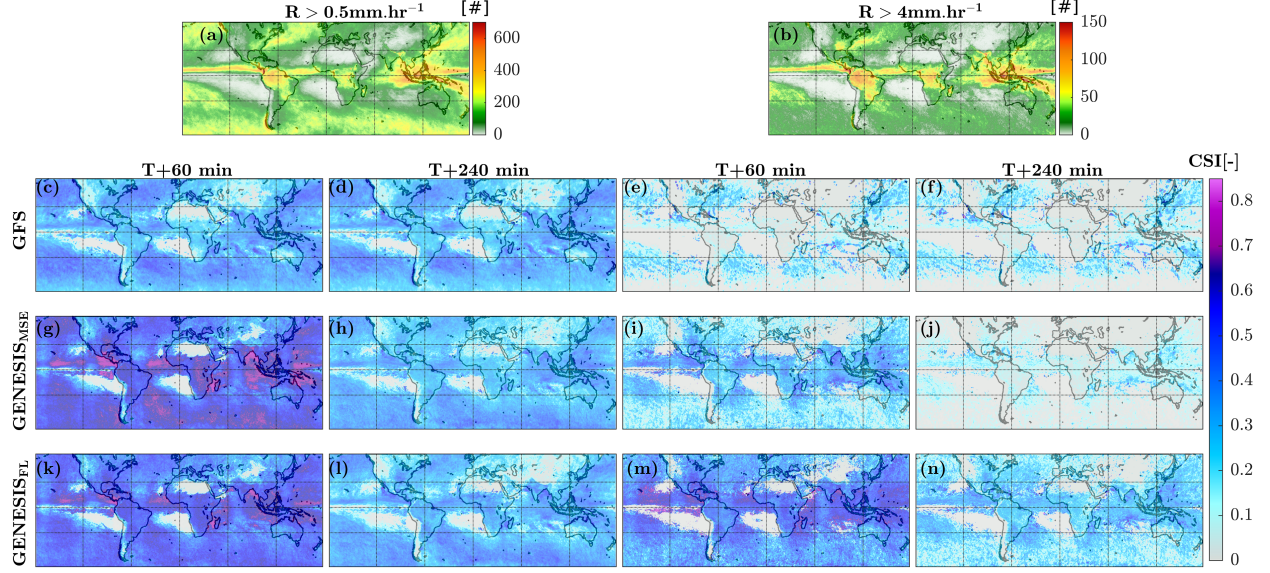


Fig. 8. Occurrence of precipitation rate above 0.5 and 4 mm hr⁻¹ (a–b) along with the associated CSI values at $T + 60$ and $T + 240$ min for GFS (c–f), GENESIS_{MSE} (g–j), and GENESIS_{FL} (k–n).

time.

As is evident, the classification network is more skillful than the others across a wider range of scales and rates. Even though the skill for rates $> 0.5 \text{ mm hr}^{-1}$ is worse than the regression network, it begins to outperform GENESIS_{MSE} as the rate increases and the scale decreases (Fig. 7 g–i). We can see that FSS ranges from 0.56 to 0.64 for rates greater than 4 mm hr⁻¹ at a 2-hour lead time, across scales 50–500 km, while both GFS and regression network are not skillful. For a 4-hour lead time and rates greater than 4 mm hr⁻¹, almost none of the nowcasts show any skills, except the GENESIS_{FL} at scale 500 km. The difference between the performance of the networks can be explained through the role of the cost function. While the MSE-loss function attempts to represent the bulk of the precipitation distribution, which is mainly populated with light rates, the FL-loss function improves the representation of high-intensity precipitation at the expense of lower scores when considering lighter rates.

4.5. Global Error Analysis

This section aims to further evaluate the performance of the nowcasting networks by conducting a quasi-global assessment using the CSI index over one year of the test data,

from April 2022 to March 2023. We can provide 48 sets of input tensor blocks (Fig. 2) to the nowcasting machines per day. To make the global analysis computationally amenable and reduce the temporal correlation between the samples, we only confine our considerations to six sampled tensor blocks per day with a four-hour interval. For comparing the results with the reference IMERG, we use the CSI at two different thresholds 0.5, and 4 mm hr⁻¹ as shown in Fig. 8. To ease the discussion in this subsection, the CSI values are referred to as high (CSI ≥ 0.50), medium ($0.25 \leq \text{CSI} < 0.50$), and low (CSI < 0.25).

The first row of Fig. 8 a–b shows the number of precipitation occurrences with rates greater than 0.5 and 4 mm hr⁻¹. Precipitation with intensity greater than 0.5 mm hr⁻¹ follows the general global pattern of precipitation occurrence with the highest rates over the Intertropical Convergence Zone (ITCZ), Amazon, and Congo rainforests, as well as the Maritime Continent where synoptic low-level convergence is the main lifting mechanism (Feng et al., 2021). Over the mid-latitudes, frequent precipitation mainly occurs over the east coast of North America, East Asia, and the Southern Ocean, where frontal lifting often drives the precipitation (Catto et al., 2012). As shown, the occurrence of precipitation with intensity greater than 4 mm hr⁻¹ is more frequent over the tropical regions within 20°S–N, where deep convective precipitation is the predominant regime (Liu et al., 2013).

Figure 8 c–f show CSI_{0.5}, and CSI₄ at the 2nd and 8th time steps for GFS forecasts. The CSI_{0.5} values at the 2nd lead time show that the GFS exhibits low (0.25) and medium (0.35) skills in capturing a large portion of the entire body of the precipitation distribution over land and oceans, respectively. However, by increasing the precipitation threshold to 4 mm hr⁻¹, the GFS skill in capturing localized and short-lived precipitation over land decreases significantly to almost zero. On the other hand, GFS shows slightly improved CSI₄ over mid-latitudes (0.15) where the extratropical cyclones and their embedded mesoscale fronts occur frequently over the Southern Ocean, east coast of North America, and East Asia.

The skill of GFS seems negligible near ITCZ. This may be caused by the misrepresentation of the position of frequent deep and small-scale convective events associated with high-level cumuliform clouds. These clouds are deep and vertically active but small and patchy with a short life cycle ($< 2\text{hr}$) (Rosenfeld and Lensky, 1998). These characteristics make the

prediction of their precipitation events location sensitive (Wallace and Hobbs, 2006; Zhang and Wang, 2021). Analogous to the previous analysis, the results show that the skill is not significantly a function of the examined lead times.

The results in Fig. 8 g–j demonstrate that the regression network has high skills in capturing precipitation rates greater than 0.5 mm hr^{-1} both over ocean and land within a 1-hour lead time with mean CSI values of 0.65 and 0.6, respectively. However, the forecast quality declines to medium when the lead time increases by three hours. For a 4 mm hr^{-1} threshold, at the 1-hour lead time, the regression network shows medium (0.48) skills over the tropics and low skills (0.25) over middle latitudes. Moreover, it can be seen that the skill is higher over the ocean than over land with mean CSI_4 values of 0.55 and 0.45, respectively, when the lead time is 1 hour. This pattern may be attributed to a more localized, intense, and transient nature of convective precipitation cells overland compared with the ocean. Increasing the lead time to 4 hours, the regression network shows almost negligible skills over the middle latitudes dominated by nimbostratus clouds giving rise to steady and continuous precipitation and low skills ($\text{CSI}_4 \approx 0.1$) over the tropics, where mostly cumulonimbus clouds produce frequent intense convective precipitation (Houze Jr, 2014).

Figure 8 k–n indicate that GENESIS_{FL} has approximately similar skill in capturing precipitation rate greater than 0.5 mm hr^{-1} compared to GENESIS_{MSE}. However, it has high skills (0.60) for 4 mm hr^{-1} threshold at a 1-hour lead time over the tropics and medium skills (0.48) over mid-latitudes. Although, by increasing the lead time to 4 hours, the skill of the classification network decreases to 0.35 and 0.20 over the tropics and mid-latitudes, it still shows a higher skill compared with the regression network in capturing heavier precipitation over both ITCZ and middle latitudes.

To gain deeper insights into the performance of the nowcasting machines, we examine the joint precipitation class distribution of the nowcasts and IMERG at the first and final lead times. This analysis is conducted using one year of test data, and the results are visualized in Fig. 9. Note that in order to construct this joint histogram, the continuous precipitation rate obtained from IMERG and the regression network are discretized into the defined classes for one-to-one comparisons. Furthermore, for each plot, three metrics including the bias, difference in standard deviation ($\Delta\sigma$), and the Wasserstein distance (wsd) are reported.

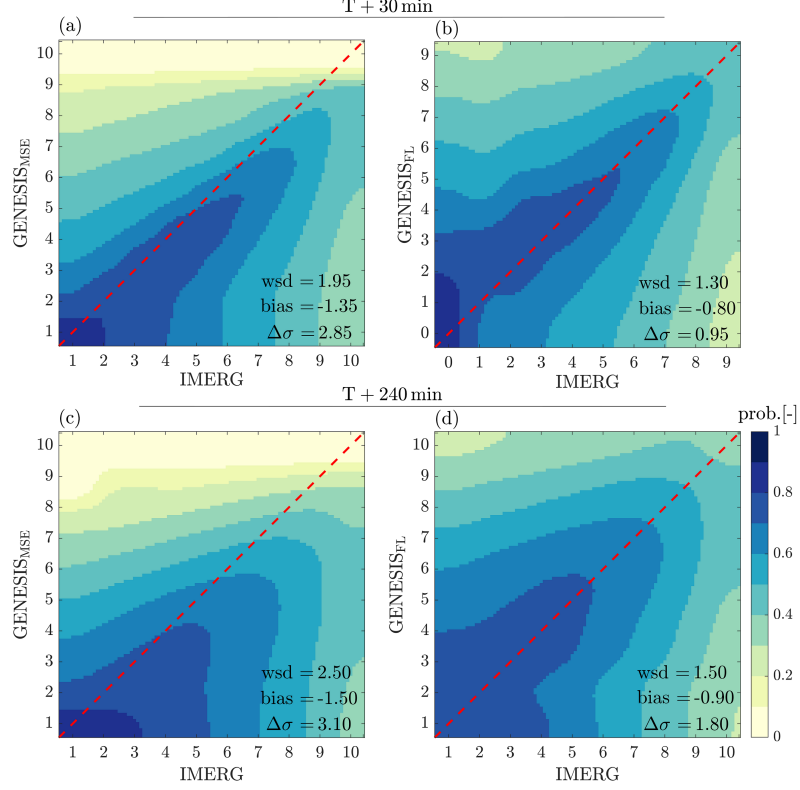


Fig. 9. Scaled joint precipitation class distribution of GENESIS_{MSE} and GENESIS_{FL} in relation to IMERG at $T + 30$ min (a–b) and $T + 240$ min (c–d). Ten classes are defined in a logarithmic scale ranging from 0.1 to 32 mm hr⁻¹, assigning rates below (above) 0.1 (32) mm hr⁻¹ to class 1 (10).

The bias and $\Delta\sigma$ are calculated as the difference between the mean and standard deviation of the observed and predicted class histograms, respectively – considering the associated rate of each class is the center of each bin.

Visual inspection (Fig. 9 a,b) shows that the regression network approximates the IMERG data well in the first four classes with a corresponding precipitation rate below 1.6 mm hr⁻¹ while the classification network has overestimation in those ranges. However, for classes with higher precipitation rates; predictions of the classification network are more consistent with the IMERG. The reported metrics reaffirm the improved performance of the classification compared with the regression network. Overall, the classification network demonstrates less underestimation (bias = -0.8 mm hr⁻¹) and a closer variability to the IMERG, compared to the regression network (bias = -1.35 mm hr⁻¹). Lower values of the Wasserstein distance also indicate that beyond the bias and variability, the classification network is more capable

to recover the entire shape of the precipitation distribution.

Increasing the lead time to 4 hours (Fig. 9 c,d) results in increased dispersion of joint histogram around the diagonal line for both regression and classification networks, which can be attributed to the blurriness effects of the convolution operator at higher lead times. Nonetheless, the classification network continues to outperform the regression network in capturing precipitation at higher rates. With a lead time increase of 3.5 hours, the Wasserstein distance from the IMERG increases by 30% for regression and 15% for classification.

5. Summary and Conclusion

In this paper, we developed the Global prEcipitation Nowcasting using intEgrated multi-Satellite retrIevalS (GENESIS) by fusing Convolutional LSTM into the U-Net architecture. The developed network can learn efficiently from the past sequences of IMERG precipitation along with past-to-future sequences of physically related variables to predict precipitation globally every 30 minutes within a 4-hour lead time. The developed network is trained using two different loss functions including mean-squared error, and focal loss to analyze their effects on capturing extreme events. The performance of the developed models is then assessed against GFS forecasts – considering the IMERG as the reference.

The results indicated that recasting the precipitation nowcasting as a classification problem using the focal loss can improve capturing the evolution of extreme events beyond a regression loss that relies on the mean-squared error. In particular, on average, the CSI₈ index increases from 0.09 (regression) to 0.25 (classification) over the entire 4 hours of lead times for the test data set. In contrast, the regression network showed improved detection of rates greater than 1 mm hr^{-1} , which are mainly dominated by less intense precipitation. This finding was further substantiated with joint histogram analysis and computing the Wasserstein distance between the precipitation nowcasts and IMERG. In particular, it was shown that the focal loss leads to improved preservation of the shape of the precipitation distribution as the lead time grows beyond the mean squared loss function.

Furthermore, it was shown that, on average, the inclusion of the physical variables, including total precipitable water and horizontal near-surface wind velocities, can improve precipitation nowcasting, as for example the recall rate was increased by 12 (20)% on average

over the 4-hours lead time in the regression (classification) network. This improvement in the regression (classification) network grows from 5 (6)% to 17 (30)% as the lead time increases from 30 minutes to 4 hours.

Multiscale analysis of the nowcasting models demonstrated that GFS forecasts are spatially skillful for predicting precipitation rates above 1 mm hr^{-1} on spatial scales $s \geq 50 \text{ km}$, while the nowcasting machines are capable of capturing those events at the native resolution of IMERG at 10 km within the 2-hour lead time. It was shown that the classification network remains skillful for intensities greater than $1 (4) \text{ mm hr}^{-1}$ at scales larger than $50 (500) \text{ km}$, on average over the entire 4-hour lead times. Also, the spatial error analysis indicated that, compared to the GFS forecasts, the nowcasting machines seem to be effective in extending short-term forecasts of tropical (convective) more than mid-latitude (frontal) precipitation events.

The following future research directions can be envisaged. First, it will be worth investigating how the inclusion of other forecast variables such as cloud liquid and ice water content as well as surface soil moisture and temperature can affect the quality of regional precipitation nowcasting. Second, efforts are needed to be devoted to improving the prediction of heavy precipitation at a long lead time perhaps by providing more high-resolution simulation/observational constraints as well as exploring new loss functions that are more adapted to the problem at hand. Third, increasing the number of classes in the classification network to enhance the accuracy of rate range estimation should be considered for future research despite the high computational cost. Fourth, it will be worth analyzing the performance of training two separate networks for tropical and mid-latitude regions as this may lead to improvements due to contrasting precipitation regimes in these regions. Lastly, to cope with the blurriness effects, one might explore embedding a super-resolution convolutional neural network into the nowcasting machine.

This paper is supported with the corresponding repository on GitHub (https://github.com/reyhaneh-92/GENESIS_Nowcast), which holds pre-trained GENESIS models and architecture written in the Python 3 programming language using the Keras deep learning library.

Acknowledgment

The first and second authors acknowledge the support from NASA’s Remote Sensing Theory program (RST, 80NSSC20K1717) through Dr. Lucia Tsaoussi, NASA’s Global Precipitation Measurement (GPM, 80NSSC22K0596), and NASA’s Interdisciplinary Research in Earth Science (IDS) program (IDS, 80NSSC20K1294) through Dr. Will McCarty. Moreover, the authors acknowledge the Minnesota Supercomputing Institute (MSI) at the University of Minnesota for providing resources that contributed to the research results reported in this paper (<https://www.msi.umn.edu/>

References

- Martín Abadi, Ashish Agarwal, Paul Barham, Eugene Brevdo, Zhifeng Chen, Craig Citro, Greg S Corrado, Andy Davis, Jeffrey Dean, Matthieu Devin, et al. Tensorflow: Large-scale machine learning on heterogeneous distributed systems. *arXiv preprint arXiv:1603.04467*, 2016.
- Pedro Abreu, M Aglietta, M Ahlers, EJ Ahn, Ivone Freire da Mota Albuquerque, D Allard, I Allekotte, J Allen, P Allison, A Almela, et al. Description of atmospheric conditions at the Pierre Auger Observatory using the global data assimilation system (GDAS). *Astroparticle Physics*, 35(9):591–607, 2012.
- Alistair Adcroft, Whit Anderson, V Balaji, Chris Blanton, Mitchell Bushuk, Carolina O Dufour, John P Dunne, Stephen M Griffies, Robert Hallberg, Matthew J Harrison, et al. The GFDL global ocean and sea ice model OM4. 0: Model description and simulation features. *Journal of Advances in Modeling Earth Systems*, 11(10):3167–3211, 2019.
- Shreya Agrawal, Luke Barrington, Carla Bromberg, John Burge, Cenk Gazen, and Jason Hickey. Machine learning for precipitation nowcasting from radar images. *arXiv preprint arXiv:1912.12132*, 2019.
- GL Austin and A Bellon. The use of digital weather radar records for short-term precipitation forecasting. *Quarterly Journal of the Royal Meteorological Society*, 100(426):658–664, 1974.

- Georgy Ayzel, Maik Heistermann, and Tanja Winterrath. Optical flow models as an open benchmark for radar-based precipitation nowcasting (rainymotion v0. 1). *Geoscientific Model Development*, 12(4):1387–1402, 2019.
- Georgy Ayzel, Tobias Scheffer, and Maik Heistermann. RainNet v1. 0: a convolutional neural network for radar-based precipitation nowcasting. *Geoscientific Model Development*, 13(6):2631–2644, 2020.
- Nikolina Ban, Juerg Schmidli, and Christoph Schär. Evaluation of the convection-resolving regional climate modeling approach in decade-long simulations. *Journal of Geophysical Research: Atmospheres*, 119(13):7889–7907, 2014.
- Dale M Barker, Wei Huang, Yong-Run Guo, AJ Bourgeois, and QN Xiao. A three-dimensional variational data assimilation system for MM5: Implementation and initial results. *Monthly Weather Review*, 132(4):897–914, 2004.
- Stanley G Benjamin, Stephen S Weygandt, John M Brown, Ming Hu, Curtis R Alexander, Tatiana G Smirnova, Joseph B Olson, Eric P James, David C Dowell, Georg A Grell, et al. A North American hourly assimilation and model forecast cycle: The Rapid Refresh. *Monthly Weather Review*, 144(4):1669–1694, 2016.
- Neill E Bowler, Clive E Pierce, and Alan W Seed. STEPS: A probabilistic precipitation forecasting scheme which merges an extrapolation nowcast with downscaled NWP. *Quarterly Journal of the Royal Meteorological Society: A journal of the atmospheric sciences, applied meteorology and physical oceanography*, 132(620):2127–2155, 2006.
- Neill EH Bowler, Clive E Pierce, and Alan Seed. Development of a precipitation nowcasting algorithm based upon optical flow techniques. *Journal of Hydrology*, 288(1-2):74–91, 2004.
- Mark Buehner and Dominik Jacques. Non-Gaussian deterministic assimilation of radar-derived precipitation accumulations. *Monthly Weather Review*, 148(2):783–808, 2020.
- JL Catto, Christian Jakob, Gareth Berry, and Neville Nicholls. Relating global precipitation to atmospheric fronts. *Geophysical Research Letters*, 39(10), 2012.

- Global Climate and Weather Modeling Branch. The GFS Atmospheric Model—NCEP Office Note 442. *Global Climate and Weather Modeling Branch: Camp Springs, MD, USA*, 2003.
- Mohammad Reza Ehsani, Ariyan Zarei, Hoshin V Gupta, Kobus Barnard, and Ali Behrangi. Nowcasting-Nets: Deep neural network structures for precipitation nowcasting using IMERG. *arXiv preprint arXiv:2108.06868*, 2021.
- Mohammad Reza Ehsani, Ariyan Zarei, Hoshin Vijai Gupta, Kobus Barnard, Eric Lyons, and Ali Behrangi. NowCasting-Nets: Representation Learning to Mitigate Latency Gap of Satellite Precipitation Products Using Convolutional and Recurrent Neural Networks. *IEEE Transactions on Geoscience and Remote Sensing*, 60:1–21, 2022.
- Ronald M Errico, Peter Bauer, and Jean-François Mahfouf. Issues regarding the assimilation of cloud and precipitation data. *Journal of the Atmospheric Sciences*, 64(11):3785–3798, 2007.
- Zhe Feng, L Ruby Leung, Nana Liu, Jingyu Wang, Robert A Houze Jr, Jianfeng Li, Joseph C Hardin, Dandan Chen, and Jianping Guo. A global high-resolution mesoscale convective system database using satellite-derived cloud tops, surface precipitation, and tracking. *Journal of Geophysical Research: Atmospheres*, 126(8):e2020JD034202, 2021.
- David Fleet and Yair Weiss. Optical flow estimation. In *Handbook of mathematical models in computer vision*, pages 237–257. Springer, 2006.
- Urs Germann and Isztar Zawadzki. Scale-dependence of the predictability of precipitation from continental radar images. Part I: Description of the methodology. *Monthly Weather Review*, 130(12):2859–2873, 2002.
- Alex Graves. Generating sequences with recurrent neural networks. *arXiv preprint arXiv:1308.0850*, 2013.
- Clément Guilloteau, Phong VV Le, and Efi Foufoula-Georgiou. Constraining the multi-scale structure of geophysical fields in machine-learning: the case of precipitation. *IEEE Geoscience and Remote Sensing Letters*, 2023.

- Jongil Han and Hua-Lu Pan. Revision of convection and vertical diffusion schemes in the NCEP Global Forecast System. *Weather and Forecasting*, 26(4):520–533, 2011.
- Lei Han, He Liang, Haonan Chen, Wei Zhang, and Yurong Ge. Convective precipitation nowcasting using U-Net Model. *IEEE Transactions on Geoscience and Remote Sensing*, 60:1–8, 2021.
- Sepp Hochreiter and Jürgen Schmidhuber. Long short-term memory. *Neural computation*, 9(8):1735–1780, 1997.
- Cathy Hohenegger, Peter Brockhaus, Christopher S Bretherton, and Christoph Schär. The soil moisture–precipitation feedback in simulations with explicit and parameterized convection. *Journal of Climate*, 22(19):5003–5020, 2009.
- Yang Hong, Kuo-Lin Hsu, Soroosh Sorooshian, and Xiaogang Gao. Precipitation estimation from remotely sensed imagery using an artificial neural network cloud classification system. *Journal of Applied Meteorology*, 43(12):1834–1853, 2004.
- Robert A Houze Jr. *Cloud dynamics*. Academic press, 2014.
- George J Huffman, David T Bolvin, Dan Braithwaite, Kuo-Lin Hsu, Robert J Joyce, Christopher Kidd, Eric J Nelkin, Soroosh Sorooshian, Erich F Stocker, Jackson Tan, et al. Integrated multi-satellite retrievals for the global precipitation measurement (GPM) mission (IMERG). In *Satellite precipitation measurement*, pages 343–353. Springer, 2020.
- Elizabeth Hunke, William Lipscomb, Philip Jones, Adrian Turner, Nicole Jeffery, and Scott Elliott. CICE, The Los Alamos sea ice model. Technical report, Los Alamos National Lab.(LANL), Los Alamos, NM (United States), 2017.
- Yunsung Hwang, Adam J Clark, Valliappa Lakshmanan, and Steven E Koch. Improved nowcasts by blending extrapolation and model forecasts. *Weather and Forecasting*, 30(5):1201–1217, 2015.
- Ian T Jolliffe and David B Stephenson. *Forecast verification: a practitioner’s guide in atmospheric science*. John Wiley & Sons, 2012.

- Robert J Joyce and Pingping Xie. Kalman filter–based cmorph. *Journal of Hydrometeorology*, 12(6):1547–1563, 2011.
- EJ Kendon, AF Prein, CA Senior, and A Stirling. Challenges and outlook for convection-permitting climate modelling. *Philosophical Transactions of the Royal Society A*, 379(2195):20190547, 2021.
- Elizabeth J Kendon, Nigel M Roberts, Catherine A Senior, and Malcolm J Roberts. Realism of rainfall in a very high-resolution regional climate model. *Journal of Climate*, 25(17):5791–5806, 2012.
- Diederik P Kingma and Jimmy Ba. Adam: A method for stochastic optimization. *arXiv preprint arXiv:1412.6980*, 2014.
- Shunji Kotsuki, Kenta Kurosawa, Shigenori Otsuka, Koji Terasaki, and Takemasa Miyoshi. Global precipitation forecasts by merging extrapolation-based nowcast and numerical weather prediction with locally optimized weights. *Weather and Forecasting*, 34(3):701–714, 2019.
- Takuji Kubota, Shoichi Shige, Hiroshi Hashizume, Kazumasa Aonashi, Nobuhiro Takahashi, Shinta Seto, Masafumi Hirose, Yukari N Takayabu, Tomoo Ushio, Katsuhiro Nakagawa, et al. Global precipitation map using satellite-borne microwave radiometers by the GSMaP project: Production and validation. *IEEE Transactions on Geoscience and Remote Sensing*, 45(7):2259–2275, 2007.
- Ashutosh Kumar, Tanvir Islam, Yoshihide Sekimoto, Chris Mattmann, and Brian Wilson. Convcast: An embedded convolutional LSTM based architecture for precipitation nowcasting using satellite data. *Plos one*, 15(3):e0230114, 2020.
- Christian D Kummerow, David L Randel, Mark Kulie, Nai-Yu Wang, Ralph Ferraro, S Joseph Munchak, and Veljko Petkovic. The evolution of the Goddard profiling algorithm to a fully parametric scheme. *Journal of atmospheric and oceanic technology*, 32(12):2265–2280, 2015.

- Yann LeCun, Yoshua Bengio, and Geoffrey Hinton. Deep learning. *nature*, 521(7553):436–444, 2015.
- Charles Lin, Slavko Vasić, Alamelu Kilambi, Barry Turner, and Isztar Zawadzki. Precipitation forecast skill of numerical weather prediction models and radar nowcasts. *Geophysical research letters*, 32(14), 2005.
- Liao-Fan Lin and Zhaoxia Pu. Improving near-surface short-range weather forecasts using strongly coupled land–atmosphere data assimilation with GSI-EnKF. *Monthly Weather Review*, 148(7):2863–2888, 2020.
- Liao-Fan Lin, Ardeshtir M Ebtehaj, Rafael L Bras, Alejandro N Flores, and Jingfeng Wang. Dynamical precipitation downscaling for hydrologic applications using WRF 4D-Var data assimilation: Implications for GPM era. *Journal of Hydrometeorology*, 16(2):811–829, 2015.
- Tsung-Yi Lin, Priya Goyal, Ross Girshick, Kaiming He, and Piotr Dollár. Focal loss for dense object detection. In *Proceedings of the IEEE international conference on computer vision*, pages 2980–2988, 2017.
- Changhai Liu, Kyoko Ikeda, Gregory Thompson, Roy Rasmussen, and Jimy Dudhia. High-resolution simulations of wintertime precipitation in the Colorado Headwaters region: Sensitivity to physics parameterizations. *Monthly Weather Review*, 139(11):3533–3553, 2011.
- Peng Liu, ChongYin Li, Yu Wang, and YunFei Fu. Climatic characteristics of convective and stratiform precipitation over the Tropical and Subtropical areas as derived from TRMM PR. *Science China Earth Sciences*, 56:375–385, 2013.
- Andrew C Lorenc, Neill E Bowler, Adam M Clayton, Stephen R Pring, and David Fairbairn. Comparison of hybrid-4DVar and hybrid-4DVar data assimilation methods for global NWP. *Monthly Weather Review*, 143(1):212–229, 2015.
- Zhifeng Ma, Hao Zhang, and Jie Liu. Focal Frame Loss: A Simple but Effective Loss for Precipitation Nowcasting. *IEEE Journal of Selected Topics in Applied Earth Observations and Remote Sensing*, 15:6781–6788, 2022.

- David JC MacKay and David JC Mac Kay. *Information theory, inference and learning algorithms*. Cambridge university press, 2003.
- John McCormac, Ankur Handa, Andrew Davison, and Stefan Leutenegger. Semanticfusion: Dense 3d semantic mapping with convolutional neural networks. In *2017 IEEE International Conference on Robotics and automation (ICRA)*, pages 4628–4635. IEEE, 2017.
- Marion Mittermaier and Nigel Roberts. Intercomparison of spatial forecast verification methods: Identifying skillful spatial scales using the fractions skill score. *Weather and Forecasting*, 25(1):343–354, 2010.
- Volodymyr Mnih, Koray Kavukcuoglu, David Silver, Andrei A Rusu, Joel Veness, Marc G Bellemare, Alex Graves, Martin Riedmiller, Andreas K Fidjeland, Georg Ostrovski, et al. Human-level control through deep reinforcement learning. *nature*, 518(7540):529–533, 2015.
- NCEP. NCEP GFS 0.25 Degree Global Forecast Grids Historical Archive. Research Data Archive at the National Center for Atmospheric Research, Computational and Information Systems Laboratory, 2021. URL https://www.emc.ncep.noaa.gov/emc/pages/numerical_forecast_systems/gfs/documentation.php.
- Lipeng Ning, Francesca P Carli, Ardeshir Mohammad Ebtehaj, Efi Foufoula-Georgiou, and Tryphon T Georgiou. Coping with model error in variational data assimilation using optimal mass transport. *Water Resources Research*, 50(7):5817–5830, 2014.
- Guo-Yue Niu, Zong-Liang Yang, Kenneth E Mitchell, Fei Chen, Michael B Ek, Michael Barlage, Anil Kumar, Kevin Manning, Dev Niyogi, Enrique Rosero, et al. The community Noah land surface model with multiparameterization options (Noah-MP): 1. Model description and evaluation with local-scale measurements. *Journal of Geophysical Research: Atmospheres*, 116(D12), 2011.
- Shigenori Otsuka, Shunji Kotsuki, and Takemasa Miyoshi. Nowcasting with data assimilation: A case of global satellite mapping of precipitation. *Weather and Forecasting*, 31(5): 1409–1416, 2016.

- Shigenori Otsuka, Shunji Kotsuki, Marimo Ohhigashi, and Takemasa Miyoshi. GSMapRIKEN Nowcast: Global precipitation nowcasting with data assimilation. *Journal of the Meteorological Society of Japan. Ser. II*, 2019.
- Xiang Pan, Yinghui Lu, Kun Zhao, Hao Huang, Mingjun Wang, and Haonan Chen. Improving Nowcasting of Convective Development by Incorporating Polarimetric Radar Variables Into a Deep-Learning Model. *Geophysical Research Letters*, 48(21):e2021GL095302, 2021.
- Jordan G Powers, Joseph B Klemp, William C Skamarock, Christopher A Davis, Jimy Dudhia, David O Gill, Janice L Coen, David J Gochis, Ravan Ahmadov, Steven E Peckham, et al. The weather research and forecasting model: Overview, system efforts, and future directions. *Bulletin of the American Meteorological Society*, 98(8):1717–1737, 2017.
- Andreas F Prein, Wolfgang Langhans, Giorgia Fosser, Andrew Ferrone, Nikolina Ban, Klaus Goergen, Michael Keller, Merja Tölle, Oliver Gutjahr, Frauke Feser, et al. A review on regional convection-permitting climate modeling: Demonstrations, prospects, and challenges. *Reviews of geophysics*, 53(2):323–361, 2015.
- Seppo Pulkkinen, Daniele Nerini, Andrés A Pérez Hortal, Carlos Velasco-Forero, Alan Seed, Urs Germann, and Loris Foresti. Pysteps: an open-source Python library for probabilistic precipitation nowcasting (v1. 0). *Geoscientific Model Development*, 12(10):4185–4219, 2019.
- William M Putman and Shian-Jiann Lin. Finite-volume transport on various cubed-sphere grids. *Journal of Computational Physics*, 227(1):55–78, 2007.
- Suman Ravuri, Karel Lenc, Matthew Willson, Dmitry Kangin, Remi Lam, Piotr Mirowski, Megan Fitzsimons, Maria Athanassiadou, Sheleem Kashem, Sam Madge, et al. Skilful precipitation nowcasting using deep generative models of radar. *Nature*, 597(7878):672–677, 2021.
- Waseem Rawat and Zenghui Wang. Deep convolutional neural networks for image classification: A comprehensive review. *Neural computation*, 29(9):2352–2449, 2017.

- Maarten Reyniers. *Quantitative precipitation forecasts based on radar observations: Principles, algorithms and operational systems*. Institut Royal Météorologique de Belgique Brussel, Belgium, 2008.
- Yoann Robin, Pascal Yiou, and Philippe Naveau. Detecting changes in forced climate attractors with Wasserstein distance. *Nonlinear Processes in Geophysics*, 24(3):393–405, 2017.
- Olaf Ronneberger, Philipp Fischer, and Thomas Brox. U-net: Convolutional networks for biomedical image segmentation. pages 234–241, 2015.
- Daniel Rosenfeld and Itamar M Lensky. Satellite-based insights into precipitation formation processes in continental and maritime convective clouds. *Bulletin of the American Meteorological Society*, 79(11):2457–2476, 1998.
- Joseph T Schaefer. The critical success index as an indicator of warning skill. *Weather and forecasting*, 5(4):570–575, 1990.
- K Schamm, M Ziese, A Becker, P Finger, A Meyer-Christoffer, U Schneider, M Schröder, and P Stender. Global gridded precipitation over land: A description of the new GPCC First Guess Daily product. *Earth System Science Data*, 6(1):49–60, 2014.
- Xingjian Shi, Zhourong Chen, Hao Wang, Dit-Yan Yeung, Wai-Kin Wong, and Wang-chun Woo. Convolutional LSTM network: A machine learning approach for precipitation nowcasting. *Advances in neural information processing systems*, 28, 2015.
- Gregor Skok and Nigel Roberts. Analysis of fractions skill score properties for random precipitation fields and ECMWF forecasts. *Quarterly Journal of the Royal Meteorological Society*, 142(700):2599–2610, 2016.
- Casper Kaae Sønderby, Lasse Espeholt, Jonathan Heek, Mostafa Dehghani, Avital Oliver, Tim Salimans, Shreya Agrawal, Jason Hickey, and Nal Kalchbrenner. Metnet: A neural weather model for precipitation forecasting. *arXiv preprint arXiv:2003.12140*, 2020.

- Juanzhen Sun. Convective-scale assimilation of radar data: progress and challenges. *Quarterly Journal of the Royal Meteorological Society: A journal of the atmospheric sciences, applied meteorology and physical oceanography*, 131(613):3439–3463, 2005.
- Juanzhen Sun, Ming Xue, James W Wilson, Isztar Zawadzki, Sue P Ballard, Jeanette Onvlee-Hooimeyer, Paul Joe, Dale M Barker, Ping-Wah Li, Brian Golding, et al. Use of NWP for nowcasting convective precipitation: Recent progress and challenges. *Bulletin of the American Meteorological Society*, 95(3):409–426, 2014a.
- Weichen Sun, Fei Su, and Leiquan Wang. Improving deep neural networks with multilayer maxout networks. In *2014 IEEE Visual Communications and Image Processing Conference*, pages 334–337. IEEE, 2014b.
- Sagar K Tamang, Ardeshir Ebtehaj, Dongmian Zou, and Gilad Lerman. Regularized variational data assimilation for bias treatment using the Wasserstein metric. *Quarterly Journal of the Royal Meteorological Society*, 146(730):2332–2346, 2020.
- Zoltan Toth and Eugenia Kalnay. Ensemble forecasting at NCEP and the breeding method. *Monthly Weather Review*, 125(12):3297–3319, 1997.
- Cédric Villani et al. *Optimal transport: old and new*, volume 338. Springer, 2009.
- Gabriele Vissio, Valerio Lembo, Valerio Lucarini, and Michael Ghil. Evaluating the performance of climate models based on Wasserstein distance. *Geophysical Research Letters*, 47(21):e2020GL089385, 2020.
- John M Wallace and Peter V Hobbs. *Atmospheric science: an introductory survey*, volume 92. Elsevier, 2006.
- Yunbo Wang, Haixu Wu, Jianjin Zhang, Zhifeng Gao, Jianmin Wang, S Yu Philip, and Mingsheng Long. Predrnn: A recurrent neural network for spatiotemporal predictive learning. *IEEE Transactions on Pattern Analysis and Machine Intelligence*, 45(2):2208–2225, 2022.

- WC Woo and WK Wong. Application of optical flow techniques to rainfall nowcasting. In *the 27th Conference on Severe Local Storms*, 2014.
- Linjie Yang, Yuchen Fan, and Ning Xu. Video instance segmentation. In *Proceedings of the IEEE/CVF International Conference on Computer Vision*, pages 5188–5197, 2019.
- Sara Q Zhang, Milija Zupanski, Arthur Y Hou, Xin Lin, and Samson H Cheung. Assimilation of precipitation-affected radiances in a cloud-resolving WRF ensemble data assimilation system. *Monthly Weather Review*, 141(2):754–772, 2013.
- Xu Zhang, Yuhua Yang, Baode Chen, and Wei Huang. Operational precipitation forecast over China using the weather research and forecasting (WRF) model at a gray-zone resolution: impact of convection parameterization. *Weather and Forecasting*, 36(3):915–928, 2021.
- Yan Zhang and Kaicun Wang. Global precipitation system size. *Environmental Research Letters*, 16(5):054005, 2021.